Mon. Not. R. Astron. Soc. **000**, 000–000 (0000) Printed 27 November 2012 (MN LATEX style file v2.2)

arXiv:1211.5966v1 [astro-ph.CO] 26 Nov 2012

Measuring the mass distribution of voids with stacked weak lensing

Yuichi Higuchi[1]⋆, Masamune Oguri[2] and Takashi Hamana[3]
[1]*Department of Astronomy, Graduate school of Science, University of Tokyo, Tokyo 113-0033, Japan*
[2]*Kavli Institute for the Physics and Mathematics of the Universe (Kavli IPMU, WPI), University of Tokyo, Chiba 277-8583, Japan*
[3]*National Astronomical Observatory of Japan, Mitaka, Tokyo 181-8588, Japan*

27 November 2012

ABSTRACT
We study the prospects for measuring the dark matter distribution of voids with stacked weak lensing. We select voids from a large set of N-body simulations, and explore their lensing signals with the full ray-tracing simulations including the effect of the large-scale structure along the line-of-sight. The lensing signals are compared with simple void model predictions to reconstruct the three-dimensional mass distribution of voids. We show that the stacked weak lensing signals are detected at significant level (S/N$\geqslant$ 5) for a 5000 degree^2 survey area, for a wide range of void radii up to $\sim$ 50 Mpc. The error from the shape noise little affects lensing signals at large scale. It is also found that dense ridges around voids have a great impact on the weak lensing signals, suggesting that proper modeling of the void density profile including surrounding ridges is essential for extracting the average total mass of voids.

Key words: gravitational lensing: weak, stacked lensing, large-scale structure of universe
LATEX – style files: `mn2e.sty`

1 INTRODUCTION

Cosmological structure formation and matter distribution of the universe depend on models of cosmology. Therefore one of the keys for constraining cosmology is to understand the distribution of matter. High density peaks in the matter density distribution which correspond to galaxies and galaxy clusters have been well studied (Broadhurst et al. 2005; Umetsu et al. 2011; Oguri et al. 2012). These overdensity regions are used for constraining cosmology (Takada 2006; Oguri & Takada 2011; Prada et al. 2012). On the other hand, low density peaks which correspond to voids have attracted less attention in spite of its long history (Kirshner et al. 1981) and the fact that they fill more than 80% of the volume of the universe and therefore are the essential component of large scale structure (LSS) of the universe.

There have been severel analytical works that studied the formation and evolution of voids (Fillmore & Goldreich 1984; Suto et al. 1984; Furlanetto & Piran 2006). The early evolution of void is well described by a spherical collapse model. In this model underdense regions expand and gradually become deep until the shell crossing occurs (Peebles 1980). Effects of different cosmology on voids have also been studied (Moffat 2006; Park & Lee 2007; Lee & Park 2009; Kamionkowski et al. 2009; Li et al. 2012). These papers pointed out possibilities for constraining cosmology with voids, including primordial non-gaussianity and modified gravity theories.

On the other hand, observationally various void finding algorithms have been applied to redshift surveys such as the Sloan Digital Sky Survey (SDSS) to study properties of voids (Strauss et al. 1992; Jones et al. 2004; Colberg et al. 2008; Pan et al. 2012). It was found that voids are significantly underdense in their observations which use galaxy distribution for searching voids. These results are broadly consistent with theoretical predictions.

However many problems still exist when comparing simulations with observations (e.g. Ryden & Turner 1984; Klypin et al. 1999; Tavasoli et al. 2012). In addition, the matter distribution of voids is estimated by assuming the galaxy bias on observations, and therefore the uncertainty of the bias is one of the most serious challenges in void studies. By contrast, gravitational lensing trace all matters regardless of baryon or dark matter. In fact, the possibility of studying voids with weak gravitational lensing was discussed in Jain & Van Waerbeke (2000), and a possible detection was made in Miyazaki et al. (2002). While lensing signals of individual voids are weak (Amendola et al. 1999), next gen-

---

⋆ E-mail: yuichi.higuchi@nao.ac.jp

eration wide field surveys such as Subaru Hyper Suprime-cam survey (HSC) (Miyazaki et al. 2006) will be able to detect such signals and study the true matter distribution in voids without any assumption of galaxy bias.

This paper is organized as follows. In Sec.2, we describe basics of our analyzing techniques, focusing on how we can obtain information of dark matter distribution from gravitational lensing. In Sec.3, we describe our simulation and void finding algorithm. In Sec.4, we describe the mass function of voids. The void model used for fitting lensing signals are presented in Sec.5. In Sec.6, we show the result of the stacking analysis and fitting with our model. We summarize our results in Sec.7.

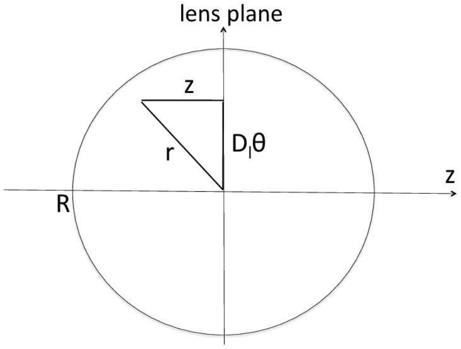

Figure 1. Definition of the coordinate system

2 BASICS OF ANALYSIS

2.1 basics of gravitational lensing

Throughout this work, we assume a spatially flat universe. Gravitational lensing effects on the α-β plane is characterized by an isotropic stretching called convergence $\kappa(\boldsymbol{\theta})$ and anisotropic distortion called shear $\gamma_1(\boldsymbol{\theta})$ and $\gamma_2(\boldsymbol{\theta})$. They are related to the two dimensional analogue of the Newtonian gravitational potential $\psi(\boldsymbol{\theta})$ as

$$\kappa(\boldsymbol{\theta}) = \frac{1}{2}\nabla^2\psi(\boldsymbol{\theta}), \tag{1}$$

$$\gamma_1(\boldsymbol{\theta}) = \frac{1}{2}\left(\frac{\partial^2\psi(\boldsymbol{\theta})}{\partial\theta_\alpha^2} - \frac{\partial^2\psi(\boldsymbol{\theta})}{\partial\theta_\beta^2}\right), \tag{2}$$

$$\gamma_2(\boldsymbol{\theta}) = \frac{\partial^2\psi(\boldsymbol{\theta})}{\partial\theta_\alpha\partial\theta_\beta}, \tag{3}$$

Then convergence at the position $\boldsymbol{\theta}$ is represented as

$$\kappa(\boldsymbol{\theta}) = \frac{3\mathrm{H_0}^2\Omega_{\mathrm{m0}}}{2\mathrm{c}^2}\frac{\mathrm{D_{ls}D_l}}{\mathrm{D_s a_l}^3}\int dz\delta(\boldsymbol{\theta},\mathrm{z}), \tag{4}$$

where z is distance from lens which are connected with distance r from the center of a lens and distance $\mathrm{D_l}|\boldsymbol{\theta}|$ on the lens plane (fig.1)

$$\mathrm{r}^2 = (\mathrm{D_l}\boldsymbol{\theta})^2 + \mathrm{z}^2,$$

$$\theta^2 = \theta_\alpha^2 + \theta_\beta^2,$$

and $\delta(\boldsymbol{\theta}, z)$ is density contrast

$$\delta(\boldsymbol{\theta}, z) = \frac{\rho(\boldsymbol{\theta}, z) - \bar{\rho}(z)}{\bar{\rho}(z)}, \tag{5}$$

with $\bar{\rho}(z)$ being the average density at z. $\mathrm{H_0}$, Ω_{m0} are hubble parameter and matter density parameter at present. c is speed of light. $\mathrm{a_l}$ is scale factor at lens position. $\mathrm{D_s}$, $\mathrm{D_l}$ and $\mathrm{D_{ls}}$ are angular diameter distance which are expressed as

$$\mathrm{D_s} = \mathrm{a_s}\chi_{\mathrm{s}}, \mathrm{D_l} = \mathrm{a_l}\chi_{\mathrm{l}}, \mathrm{D_{ls}} = \mathrm{a_s}(\chi_{\mathrm{s}} - \chi_{\mathrm{l}}), \tag{6}$$

where $\mathrm{a_s}$ is scale factor at source position. $\chi_{\mathrm{s}}, \chi_{\mathrm{l}}$ are comoving distance from observer to source and lens.

It is useful to introduce the tangential distortion component γ_+ and the cross component $\gamma_\times$ which is rotated by 45°. The tangential shear components include all information of lens, if a lensing mass profile is axisymmetric on sky. These two components are defined with γ_1 and γ_2 as

$$\begin{pmatrix}\gamma_+ \\ \gamma_\times\end{pmatrix} = \begin{pmatrix}-\cos2\eta & -\sin2\eta \\ -\sin2\eta & \cos2\eta\end{pmatrix}\begin{pmatrix}\gamma_1 \\ \gamma_2\end{pmatrix}, \tag{7}$$

where η is the angle between axis-α and $\boldsymbol{\theta}$. The sign of tangential shear indicate that background galaxy shape becomes tangentially deformed for positive and radially deformed for negative with respect to the lens center.

Weak lensing signal is small so that it is difficult to measure masses down to low mass objects. However, by stacking lensing signals from many samples, we can reduce errors which limit to obtain information on the objects (e.g. Mandelbaum et al. 2006; Okabe et al. 2010; Oguri et al. 2012). Therefore stacked lensing is a powerful tool for measuring average dark matter distributions of targets. The stacked lensing technique is also used to constrain cosmological parameters (e.g. Oguri & Takada 2011; Rozo et al. 2010). In the weak lensing limit, the average tangential shear profile at θ_i is related to the convergence (Bartelmann & Schneider 2001) as

$$\langle\gamma_+\rangle(\theta_{\mathrm{i}}) = \bar{\kappa}(\theta < \theta_{\mathrm{i}}) - \langle\kappa\rangle(\theta_{\mathrm{i}}), \tag{8}$$

where $\langle\cdots\rangle$ denotes average value in the circular annulus, the first term is the mean convergence within a circular aperture of radius θ_{i} defined as

$$\bar{\kappa}(\theta < \theta_{\mathrm{i}}) = \frac{1}{\pi\theta_{\mathrm{i}}^2}\int_{\theta\leqslant\theta_{\mathrm{i}}} d\boldsymbol{\theta}'\kappa(\boldsymbol{\theta}'), \tag{9}$$

and the second term is the mean convergence in the i-th radial bin. The average cross shear component $\langle\gamma_\times\rangle(\theta < \theta_i)$ must be zero in weak lensing.

In stacked lensing method, the following statistical uncertainty on tangential shear should be considered

$$\sigma_{\gamma_+}^2 = \sigma_{\mathrm{void}}^2 + \sigma_{\mathrm{LSS}}^2 + \sigma_{\mathrm{shape}}^2, \tag{10}$$

where σ_{void}^2 is the statistical error coming from the deference in the structure of each void used in stacking analysis, σ_{LSS}^2 is the error coming from large-scale structure along the line-of-sight and $\sigma_{\mathrm{shape}}^2$ is the shape noise error coming from the intrinsic ellipticity of galaxies used for weak lensing measurements. Considering errors coming from structure of voids and LSS, the covariance matrix between i-th and j-th radial bin is estimated as

$$\sigma^2_{\gamma_+(\theta_\mathrm{i},\theta_\mathrm{j})} = \frac{\sum_l^{\mathrm{N_v}} (\gamma_{+,l}(\theta_\mathrm{i}) - \langle\gamma_+(\theta_\mathrm{i})\rangle)(\gamma_{+,l}(\theta_\mathrm{j}) - \langle\gamma_+(\theta_\mathrm{j})\rangle)}{\mathrm{N_v}}, \tag{11}$$

where $\gamma_{+,l}(\theta_\mathrm{i})$ is the value of tangential shear in the l-th void at i-th radial bin and $\mathrm{N_v}$ is the number of voids. In addition to this, the error from intrinsic ellipticity shown in Van Waerbeke et al. (2000) is determined as

$$\sigma^2_{\mathrm{shape}} = \frac{\sigma^2_\epsilon}{\mathrm{N_v n_g S}}, \tag{12}$$

where σ_ϵ is the rms amplitude of the intrinsic ellipticity distribution, $\mathrm{n_g}$ is the number density of galaxies and S is the area of a bin. Throughout this paper we adopt $\sigma_\epsilon = 0.4$ and $n_g = 30$ arcmin^{-2} assuming survey parameters in the HSC survey. Shape noise becomes the dominant error at only small scale, on the other hand the other errors becomes dominant at large scale (sec.6.5). We ignore other observational systematics such as imperfections in the telescope and electric devices of detectors.

2.2 Signal to noise ratio of stacked lensing

A useful way to quantify the observability is to calculate the total Signal-to-Noise (S/N) ratio over the considered scale. Our calculation follows Oguri & Takada (2011). The total S/N is expressed as

$$\left(\frac{\mathrm{S}}{\mathrm{N}}\right)^2 = \sum_{\mathrm{i,j}} \gamma_+(\theta_\mathrm{i}) \left[\mathrm{cov}(\gamma_+(\theta_\mathrm{i}), \gamma_+(\theta_\mathrm{j}))\right]^{-1} \gamma_+(\theta_\mathrm{j}), \tag{13}$$

where the summation indices i, j run over radial bins. For calculation with the tangential shear we estimate S/N for both situations that covariance matrix include and does not include the shape noise. For calculation with convergence we can replace γ_+ with κ in eq.13. The covariance matrix does not include the shape noise for this case.

The S/N is related to the accuracy of the mass estimate. More specifically, they are related as (Oguri & Takada 2011)

$$\frac{\Delta\mathrm{M}}{\mathrm{M}} \sim \left(\frac{\mathrm{S}}{\mathrm{N}}\right)^{-1} \left(\frac{d\ln\gamma_+}{d\ln\mathrm{M}}\right)^{-1}. \tag{14}$$

Therefore S/N is proportional to the accuracy for constraining the mass of the object.

2.3 Mass reconstruction

It is sometimes useful to derive a model independent information of the mass from weak lensing data (e.g. Okabe et al. 2010; Squires et al. 1996 and Squires et al. 1997). Convergence in each circular annulus of radius θ is related to the projected mass density

$$\kappa(\theta) = \frac{\Sigma(\theta)}{\Sigma_{cr}}, \tag{15}$$

where Σ_cr is critical projected mass density defined as

$$\Sigma_\mathrm{cr} = \frac{\mathrm{c}^2}{4\pi\mathrm{G}} \frac{\mathrm{D_s}}{\mathrm{D_l D_{ls}}}. \tag{16}$$

The mass is related to convergence (Bartelmann & Schneider 2001) as

$$\mathrm{M}(<\theta) = \int d\theta'^2 \kappa(\theta') \mathrm{U}(\theta' - \theta), \tag{17}$$

where $\mathrm{U}(\theta)$ is weight function and we adopt $\mathrm{U}(\theta) = 1$ in our calculation. When we estimate void masses which are removed from underdensity regions, we calculate those only for the region with $\kappa(\theta) < 0$. For the reconstruction from tangential shear, more careful calculation called ζ-statistics (Fahlman et al. 1994; Clowe et al. 2000) is needed.

Furthermore the mass is related to the average mass density $\bar\rho$ and void radius R

$$\begin{aligned} \mathrm{M} &= \left| \frac{4}{3}\pi\mathrm{R}^3\bar\rho - \frac{4}{3}\pi\mathrm{R}^3\rho \right| \\ &= \left| \frac{4}{3}\pi\mathrm{R}^3(\bar\rho - \rho) \right| \\ &= \frac{4}{3}\pi\mathrm{R}^3\bar\rho \mid \delta \mid, \end{aligned} \tag{18}$$

where we assume the mass density ρ is constant in the region.

3 SIMULATION

3.1 Raytracing simulation

We use a large set of ray-tracing simulation which are carried out in Sato et al. (2009). To carry out N-body simulation, they use the parallel Tree-Particle Mesh code Gadget-2 (Springel 2005 and see Sato et al. 2009 for simulation details). The simulation employ 256^3 particles in a cubic box of $240h^{-1}$ Mpc on a side. Cosmological parameters are assumed as hubble parameter $\mathrm{H_0} = 73.2$ km/s/Mpc, matter density $\Omega_\mathrm{m} = 0.238$, baryon density $\Omega_\mathrm{b} = 0.042$, dark energy density $\Omega_\Lambda = 0.762$, equation of state parameter $\mathrm{w} = -1$, spectral index $\mathrm{n_s} = 0.958$ and variance of density fluctuation with 8 h^{-1} Mpc $\sigma_8 = 0.76$. These cosmological parameters follows WMAP 3-year results (Spergel et al. 2007).

By using results of N-body simulation, they carry out ray-tracing simulation with the algorithm developed in White & Hu (2000) and Hamana & Mellier (2001). They set source redshift $\mathrm{z_s}$ at $\mathrm{z_s} \simeq 1.0$ and make 200 realizations. The FOV in each run is 5×5 degree^2. Therefore the total area is 5000 degree^2.

Here we outline the ray-tracing simulation briefly, see Sato et al. (2009) for more details. To obtain lensing signal, distance between observer and sources is divided into several regions to create set 19 lens planes separated by $120h^{-1}$ Mpc in comoving distance. Then the three dimensional density fluctuation in each each region is projected onto each lens plane. Next they trace 2048^2 rays backwards from the observer to the source plane. The initial ray directions are set on 2048^2 grids with a grid space of 0.15 arcmin. Raytracing realizations of underlying density field are made by randomly shifting the simulation boxes assuming periodic boundary conditions. The lens planes from the same box are shifted in the same way in order to maintain the clustering pattern of mass distribution in one box.

3.2 VoidFinder

For searching voids in the simulation data, we use the code called Void Finder which is publicly available (Foster & Nelson 2009). The void finding algorithm is based on Hoyle & Vogeley (2004) and Hoyle et al. (2005).

At first galaxies in halo catalogue are separated into wall galaxies which are closer than the parameter R_3 and other galaxies called field galaxies. The average distance to the third nearest galaxy D_3 and the standard deviation σ_3 are calculated from halo catalogue, and R_3 is defined as

$$R_3 = D_3 + \lambda\sigma_3, \tag{19}$$

where λ is dimensionless free parameter. λ and minimum void radius ξ affect the number and size of voids (see sec.6.1). In this paper, we adopt $\lambda = 2.0$, the same value used in Foster & Nelson (2009). Wall galaxies are then set into cubic cell of $R_3/2$ on a side. The void finder finds the center of each empty cell.

Secondly the maximal sphere are searched. Each empty cell is considered to be a part of void. The void finder sets it as a center of void, find the nearest galaxy and grow the sphere until a galaxy is on the edge. Next the void finder finds the vector connecting the center and the nearest galaxy, and mov away from the first galaxy along its vector and grow the radius of the sphere until the second nearest galaxy is on the edge. The vector connecting the center to the midpoint between the first and second galaxy is set. In a similar fashion to the second growth, the center along the vector is moved and the radius is grown until the third nearest galaxy is on the edge. In this algorithm voids are allowed to exist outside the boundary by extending it by 5 $\sim$ 10 Mpc.

Thirdly spheres which are found above are classified. The spheres are sorted from the largest to the smallest. The largest one is a void if the radius is lager than ξ. At first we consider only spheres whose radius exceed ξ. If a sphere overlaps other void by more than $\beta = 10\%$ in volume, it is merged with that void. If not, it is defined as a new void. If a sphere overlaps more than two voids by more than $\beta_3 = 2\%$ in volume, it is rejected. Next we consider spheres whose radius is smaller than ξ. Similaly, if a small sphere overlaps more than two large spheres by more than β_3, it is rejected. If it overlaps one void by more than β=50%, it is merged with the void. By this process, shape of voids may change into aspherical shape.

In this paper, we find voids that exist in the redshift range from $z = 0$ to $z = 1$ in the simulation with this void finding algorithm. The void finder is applied to halos whose masses are more than $2.2 \times 10^{12} M_\odot$ in the simulation. The total number of halos in the total FOV= 5000 degree^2 is 1.2×10^7 within $0 \leqslant z \leqslant 1$. Therefore the number density is about 2000 degree^{-2}. Then we use same parameters which are recommended in Foster & Nelson (2009) except the parameter of voids minimum radius in the process of void finding algorithm. We set minimum radius with 5 Mpc and 10 Mpc and check the effect of changing the minimum radius.

For stacked lensing analysis, we use voids with the radii between $R = 15 \sim 45$ Mpc and in the redshift range $z = 0.4 \sim 0.6$ because lensing efficiency is expected to be high at the redshift range. The number of halos for selecting voids is 2.5×10^6 in the redshift range. Then for comparison, we also use voids with $R = 15 \sim 40$ Mpc in the redshift range $z = 0.1 \sim 0.3$. The number of halos used in this redshift range is 6.0×10^5.

4 PRESS-SCHECHTER THEORY

For predicting the number count of voids, we use the modified Press-Schechter (PS) formalism (see e.g. Kamionkowski et al. 2009).

In the PS theory (Press & Schechter 1974), regions which exceed the spherical collapse linear overdensity $\delta_c = 1.689$ become halos. The probability which has the linear density fluctuation δ above δ_c becomes as

$$P(\delta > \delta_c|M) = \frac{1}{\sqrt{2\pi}}\frac{\sigma(R)}{\delta_c}\exp\left(-\frac{\delta_c^2}{2\sigma^2(R)}\right), \tag{20}$$

where M is a halo mass defined with a radius R as,

$$M = \frac{4\pi}{3}\bar{\rho}R^3, \tag{21}$$

and $\sigma^2(R)$ is the rms density fluctuation defined as,

$$\sigma^2(R) = \int \frac{dkk^2}{2\pi^2} W^2(kR)P(k), \tag{22}$$

where $W(kR)$ is the Fourier transform of the window function and $P(k)$ is the matter power spectrum. Therefore the mass function n(M) is reduced as

$$\begin{aligned} &n(M)dM \\ &\quad = 2\bar{\rho}\,|P(\delta > \delta_c|M) - P(\delta > \delta_c|M + dM)| \\ &\quad = \sqrt{\frac{2}{\pi}}\frac{\bar{\rho}}{M^2}\left|\frac{d\ln\sigma(R)}{d\ln M}\right|\frac{\delta_c}{\sigma(R)}\exp\left(-\frac{\delta_c^2}{2\sigma^2(R)}\right)dM. \end{aligned} \tag{23}$$

In order to estimate the number count of voids based on the modified PS theory, we replace δ_c in eq.23 to linear underdensity $|\delta_v|$.

In our calculation, gaussian window function and BBKS (Bardeen et al. 1986) as transfer function are used. Void masses M_v are estimated from the weak lensing signals with eq.18. For estimating the number count at a given redshift, the linear density fluctuation δ_v is evolved by using a linear growth factor.

5 VOID MODEL

Density profiles of voids are studied in previous works (e.g. Sheth & van de Weygaert 2004; Pan et al. 2012). These works indicate that in the under density region matter density is almost constant and there is a very sharp spike called a ridge near the edge of voids.

In order to make a simple void model which include properties found in the previous works, we consider a spherically symmetric void model including ridges, named double top-hat model (fig.2). One is for expressing voids, and the other is for expressing ridges. In this model, we set mass density $\rho(r)$ as

$$\rho(r) = \begin{cases} \rho_1 & (r < R_1), \\ \rho_2 & (R_1 < r < R_2), \\ 0 & (r > R_1), \end{cases} \tag{24}$$

where ρ_1 and ρ_2 are constant in each region. We assume that the total mass between the void region and the ridge region should follow the mass conservation law. The mass between two regions is related as

$$\frac{4}{3}\pi {\rm R_1}^3(\bar{\rho}-\rho_1)=\frac{4}{3}\pi({\rm R_2}^3-{\rm R_1}^3)(\rho_2-\bar{\rho}). \tag{25}$$

From eq.25, ρ_2 is expressed with ρ_1, $\rm R_1$ and $\rm R_2$

$$\rho_2=\bar{\rho}+\frac{1}{1-({\rm R_2/R_1})^3}(\rho_1-\bar{\rho}). \tag{26}$$

From eq.24 and eq.26, density contrast is reduced as

$$\delta({\rm r})=\begin{cases}\delta & ({\rm r}<{\rm R_1}),\\ \frac{\delta}{1-({\rm R_2/R_1})^3} & ({\rm R_1}<{\rm r}<{\rm R_2}),\\ 0 & ({\rm r}>{\rm R_2}).\end{cases} \tag{27}$$

An advantage of this double top-hat model is that its lensing properties can be computed analytically. By using eq.4 and eq.27, convergence becomes as

$$\begin{aligned}\kappa(\theta)=&\frac{3{\rm H_0}^2\Omega_{\rm m0}}{2{\rm c}^2}\frac{\rm D_{ls}D_l}{{\rm D_s a_l}^3}\int_{-{\rm D_l}\sqrt{{\theta_2}^2-\theta^2}}^{{\rm D_l}\sqrt{{\theta_2}^2-\theta^2}}dz\,\Big\{\delta\Theta({\rm R_1}-{\rm r})\\ &+\frac{\delta}{1-({\rm R_2/R_3})^3}\Theta({\rm r}-{\rm R_1})\Theta({\rm R_2}-{\rm r})\Big\}\\ =&\frac{3{\rm H_0}^2\Omega_{\rm m0}}{2c^2}\frac{\rm D_{ls}D_l}{{\rm D_s a_l}^3}\cdot 2\delta{\rm D_l}\cdot\\ &\left[\left\{\frac{\sqrt{{\theta_2}^2-\theta^2}-\sqrt{\theta_1^2-\theta^2}}{1-(\theta_2/\theta_1)^3}+\sqrt{\theta_1^2-\theta^2}\right\}\Theta(\theta_1-\theta)\right.\\ &\left.+\left\{\frac{\sqrt{\theta_2^2-\theta^2}}{1-(\theta_2/\theta_1)^3}\right\}\Theta(\theta-\theta_1)\Theta(\theta_2-\theta)\right],\end{aligned} \tag{28}$$

where $\Theta(r)$ is step function. The radii are related to angles

$$r = {\rm D_l}\theta, \tag{29}$$

$${\rm R_i} = {\rm D_l}\theta_{\rm i}, \tag{30}$$

where the induce i takes 1 or 2.

In addition to the analytical expression of convergence, we can also calculate the tangential shear analytically. From eq.8, the tangential shear is reduce as

$$\begin{aligned}\langle\gamma_+\rangle(\theta) &= \bar{\kappa}(<\theta)-\langle\kappa\rangle(\theta)\\ &= \frac{2}{\theta^2}\int_0^\theta d\theta'\theta'\kappa(\theta')-\langle\kappa\rangle(\theta).\end{aligned} \tag{31}$$

From eq.28, the integration becomes

$$\begin{aligned}\int_0^\theta d\theta'\theta'\kappa(\theta') =&\\ &\left\{\frac{\rm A}{3}\frac{(\theta_2/\theta_1)^3(\theta_1^2-\theta^2)^{\frac{3}{2}}-(\theta_2^2-\theta^2)^{\frac{3}{2}}}{1-(\theta_2/\theta_1)^3}\right\}\Theta(\theta_1-\theta)\\ &-\left\{\frac{\rm A}{3}\frac{(\theta_2^2-\theta^2)^{\frac{3}{2}}}{1-(\theta_2/\theta_1)^3}\right\}\Theta(\theta-\theta_1)\Theta(\theta_2-\theta)\\ &+0\cdot\Theta(\theta-\theta_2),\end{aligned} \tag{32}$$

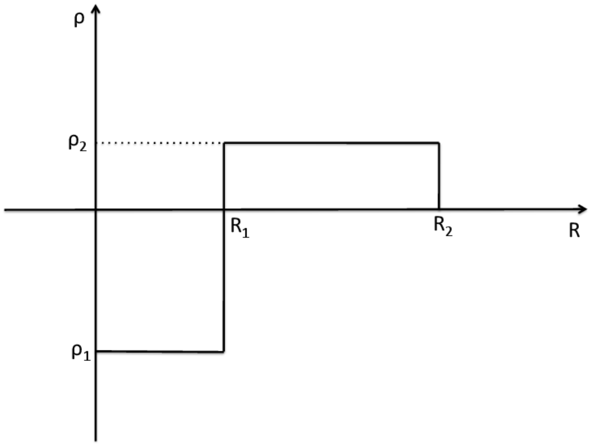

Figure 2. Double top-hat void model. In $\rm r < R_1$, $\rho(\rm r)$ equal to constant ρ_1, and $\rm R_1 < R < R_2$, $\rho(\rm r)$ equal to constant ρ_2. Relative amplitudes between ρ_1 and ρ_2 are determined from mass conservation law. Outside $\rm R_2$, ρ becomes zero.

where ${\rm A}=\frac{3{\rm H_0}^2\Omega_{\rm m0}}{{\rm c}^2}\frac{\rm D_{ls}D_l^2}{{\rm D_s a_l}^3}\delta$. Therefore with eq.28 and eq.32, analytical expression of tangential shear is reduced as

$$\begin{aligned}\langle\gamma_+\rangle(\theta) =&\\ &\left[\frac{\rm A}{3\theta^2}\frac{1}{1-(\theta_2/\theta_1)^3}\left\{(\theta_2/\theta_1)^3(2\theta_1^2+\theta^2)\sqrt{\theta_1^2-\theta^2}\right.\right.\\ &\left.\left.-(2\theta_2^2+\theta^2)\sqrt{\theta_2^2-\theta^2}\right\}\right]\Theta(\theta_1-\theta)\\ &-\left\{\frac{\rm A}{3\theta^2}\frac{(2\theta_2^2+\theta^2)\sqrt{\theta_2^2-\theta^2}}{1-(\theta_2/\theta_1)^3}\right\}\Theta(\theta-\theta_1)\Theta(\theta_2-\theta)\\ &+0\cdot\Theta(\theta-\theta_2).\end{aligned} \tag{33}$$

We assume the density contrast is equal to zero outside the second top-hat. Therefore the convergence and the tangential shear must be zero in that region.

To extract parameters from simulations, we adopt the χ^2 method. The estimator χ^2 is as follows

$$\begin{aligned}\chi^2 =& \sum_{i,j}\left(\gamma_{+,\rm model}(\theta_i)-\gamma_{+,\rm sim}(\theta_i)\right)\\ &\times\left[\mathrm{cov}(\gamma_{+,\rm sim}(\theta_i),\gamma_{+,\rm sim}(\theta_j))\right]^{-1}\\ &\times\Big(\gamma_{+,\rm model}(\theta_j)-\gamma_{+,\rm sim}(\theta_j)\Big),\end{aligned} \tag{34}$$

where $\gamma_{+,\rm model}(\theta_i)$ and $\gamma_{+,\rm sim}(\theta_i)$ are tangential shear in the model and simulation at i-th radial bin.

6 RESULT

6.1 Number count of voids

In order to check the dependence of the void number count on the parameter minimum radius ξ in the void finder, we run void finder with $\xi = 5$ Mpc and $\xi = 10$ Mpc.

Figure.3 shows histogram as a function of radius of voids for $\xi = 5$ Mpc and $\xi = 10$ Mpc for the redshift range $0 \leqslant z \leqslant 1$. We can see the dependence on the minimum radius ξ. The lager minimum radius is, the less number count

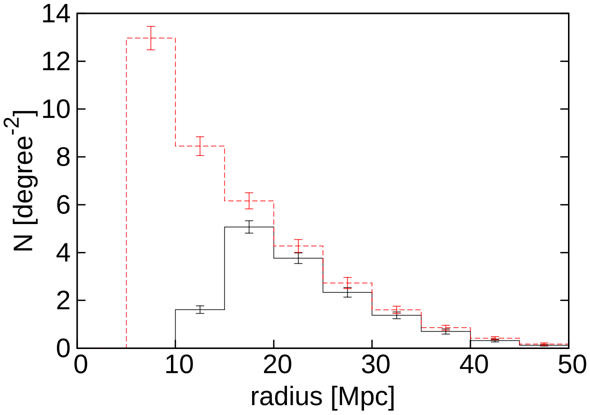

Figure 3. Number count of voids in the simulation for the redshift range $0 \leqslant z \leqslant 1$. x-axis is void radius. y-axis is number count of void in each bin. The dashed line and solid line histogram show the number count with minimum radius $\xi = 5$ Mpc and $\xi = 10$ Mpc. Error bar shows 1σ with 200 realizations.

of voids becomes. By using smaller minimum radius, we can obtain small voids which are not detected as voids with lager minimum radius. Therefore the number count of voids increases because the probability of piling up with other voids increases. This trend matches Foster & Nelson (2009). However voids which have small radii in this calculation might not be true voids, because of the strong dependence with respect to the number count of voids on the value ξ. In the stacking analysis, we set the minimum radius $\xi = 5$ Mpc. Figure.3 indicate that the number count of voids in the radius range we consider in this paper (> 15 Mpc) does not depend strongly on the choice of the minimum radius.

6.2 Direct estimate of void masses

In order to estimate mass profiles and void masses, we stack lensing signals from voids selected by the void finder. From result of stacking and eq.17, we estimate the mass in each void sample.

In sec.6.1 we obtained the number count of voids as a function of raius. We classify these voids into 6 bins based on the radii determined by the void finder. We select only voids that exist in the redshift range $z = 0.4 \sim 0.6$. We match centers of voids determined by the void finder and stack those in each bin. The radii and number of voids used for stacking analysis are showed in table.1. Points with errors in figure.4 and figure.5 show stacked convergence and tangential shear profiles in each radius.

The void masses we estimate from the convergence profiles and eq.18 are presented in table.1. The calculation is carried out only for the region $\kappa(\theta) < 0$. We find that void masses that are directly estimated from the convergence profiles are comparable to typical cluster masses ($\sim 10^{14} M_\odot$). As we will see below, these void masses are smaller than true removed masses of the voids because of the effect of surrounding ridges.

Table 1. Details of stacking. Column (1): radius of voids determined by the void finder; Column(2): the number count of voids in the each radial bin and the redshift range $z_l = 0.4 \sim 0.6$; Column(3): void mass calculated by integrating the $\kappa(\theta) < 0$ region.

Radius [Mpc]	Number of voids	Mass from $\kappa(\theta) < 0$ [$M_\odot$]
$15 \sim 20$	5246	9.03×10^{13}
$20 \sim 25$	3892	4.45×10^{14}
$25 \sim 30$	2446	1.81×10^{15}
$30 \sim 35$	1400	3.06×10^{15}
$35 \sim 40$	724	4.01×10^{15}
$40 \sim 45$	320	3.26×10^{15}

6.3 Fitting the convergence profile

In order to compute convergence and tangential shear profile of voids analytically, we put a model named double top-hat model (sec.5). We consider the source at $z_s = 1.0$, the lens at $z_l = 0.5$. For our model, we set δ, θ_1 and θ_2 in eq.28 and eq.33 as free parameters to fit stacked lensing signals in our simulation. First we ignore shape noise and only consider noise from LSS and structures of voids in the process of fitting. Fitting is performed in the parameter range $-1 \leqslant \delta \leqslant 0$, $0' \leqslant \theta_1 \leqslant 100'$, $0' \leqslant \theta_2 \leqslant 300'$. We sum up χ^2 over the radius range $0 \leqslant \theta \leqslant 90$ arcmin for $15 \leqslant R \leqslant 30$ Mpc, and $0 \leqslant \theta \leqslant 180$ arcmin for $30 \leqslant R \leqslant 45$ Mpc.

Fig.4 shows convergence profiles in simulation and the model. Model fitting is carried out for convergence profiles. We find that our simple model reconstructs lensing signals in simulation well. Best-fit parameters used in this plot are shown in table.2. Using these parameters, we estimate total void masses, i.e. the total mass removed from the void region (table.2). Our model almost fits both convergence and tangential shear profile except the radius range $15 \leqslant R \leqslant 20$ Mpc. There are two reasons why fitting fails for the smallest void radius bin. The first reason is a problem of finding voids. As we and Foster & Nelson (2009) showed, the number of voids is sensitive to minimum radius ξ in void finder. Therefore the void finder fails to find true voids which have small radii. The second reason is the violation of the mass conservation law. The mass conservation law is violated for simulated convergence profile presumably because of the large contaminations in the void catalogue at the small radius bin.

Compared with total void masses calculated from fitting of convergence profile with that from our model, masses estimated from direct integration at $\kappa(\theta) < 0$ is a few times smaller. This is because observed convergence value is cumulative value from sources to an observer. Therefore when we calculate mass we should consider the effect from the ridge outside the void. Otherwise we underestimate total void mass. In addition, the size of underdense regions in the simulation and the model are smaller than radii defined in the void finder. This is probably because the halo catalogue we use for void finding does not exactly trace the underlying matter distribution.

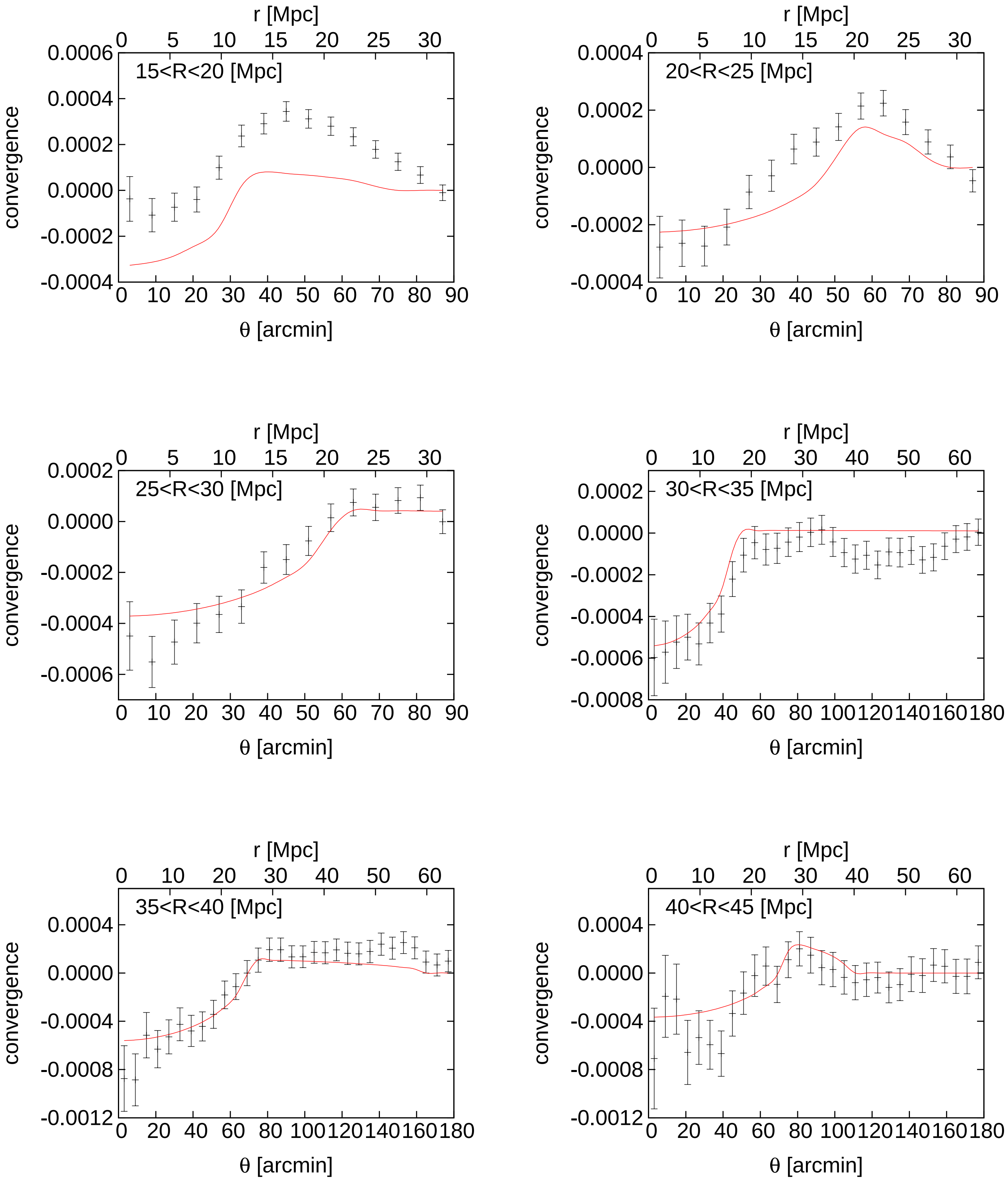

Figure 4. Stacked convergence profiles estimated from simulation (points with errors) , the best-fit double top-hat model (solid line), assuming the survey area of 5000 deg^2, the bin size $\Delta\theta = 6$ arcmin and lens redshift $z_l = 0.5$. Stacking analysis are carried out in each radius derived from the void finder; $15 \leqslant R \leqslant 20$ Mpc (*top-left*); $20 \leqslant R \leqslant 25$ Mpc (*top-right*); $25 \leqslant R \leqslant 30$ Mpc (*middle-left*); $30 \leqslant R \leqslant 35$ Mpc (*middle-right*); $35 \leqslant R \leqslant 40$ Mpc (*bottom-left*); $40 \leqslant R \leqslant 45$ Mpc (*bottom-rihgt*). Best-fit parameters are summarized in table.2.

Table 2. Best fit parameters and derived total void mass. These parameters are determined from convergence profiles. Column (1): radius of void determined with the void finder; Column (2): density contrast; Column (3): radius of underdense region; Column (4): radius of overdense region; Column (5): void mass derived from the double top-hat model

Radius in the void finder [Mpc]	δ	$D_l\theta_1$ [Mpc]	$D_l\theta_2$ [Mpc]	Void mass [$M_\odot$]
$15 \sim 20$	-0.390	12.1	25.5	1.46×10^{15}
$20 \sim 25$	-0.194	19.1	27.5	2.83×10^{15}
$25 \sim 30$	-0.244	21.0	63.0	4.78×10^{15}
$30 \sim 35$	-0.424	16.6	109	4.09×10^{15}
$35 \sim 40$	-0.316	25.5	59.8	1.10×10^{16}
$40 \sim 45$	-0.220	27.3	38.9	2.73×10^{16}

6.4 Fitting the tangential shear profile

We also use tangential shear profile for finding best-fit parameters. As we have done for convergence, we set same condition for searching best-fit parameters.

Figure.5 shows tangential shear profiles in simulations and best-fit models. Table.3 shows best-fit parameters and total void masses determined from the fitting. Total void masses are estimated with eq.18 as we have done in sec.6.3. We find that the best-fit parameters and the resulting total void masses are very similar to those obtained from fitting convergence profiles (table.2), suggesting the consistency of our analysis.

6.5 Signal-to-Noise ratio

Using the stacked lensing covariance matrix we derived, we estimate S/N for convergence and tangential shear. For tangential shear, S/N is estimated in the case of with and without the shape noise.

Fig.6 shows tangential shear profiles in both cases when the shape noise is added and not added to the covariance matrix. For illustrative purpose, points are shifted by 2 arcmin. Stacking analysis are carried out for voids in the radial range $20 \leqslant R \leqslant 25$ Mpc and the redshift range $z_l = 0.4 \sim 0.6$. The shape noise is estimated from eq.12. The error from the shape noise is added to the diagonal elements of the covariance matrix. The effect from the shape noise becomes a dominant component of the error at small scale, because the number of galaxies in each radial annulus is proportional to the radius under the condition that radial bin size Δr is constant. Over the scale we consider, however, fig.6 shows that the shape noise is not a dominant component of the error.

Total S/N is estimated for voids in the redshift ranges $z_l = 0.4 \sim 0.6$ and $z_l = 0.1 \sim 0.3$ by using eq.13. Table.4 shows S/N in the redshift range $z_l = 0.4 \sim 0.6$ for convergence, tangential shear without and with the shape noise as a function of radius. Table.5 shows S/N in the redshift range $z_l = 0.1 \sim 0.3$. Table.4 and table.5 show that the staked lensing signals are detected at significant level (S/N$\geqslant$ 5). Adding the shape noise degrades S/N, but the effect is relatively minor. Compared with total S/N in the redshift range $z_l = 0.4 \sim 0.6$, total S/N in the redshift range $z_l = 0.1 \sim 0.3$ are degraded. The error coming from structure of each void increases because the number of voids decrease as the redshift range becomes low. However, S/N for individual void in the redshift range $z_l = 0.1 \sim 0.3$ is higher than that in the redshift range $z_l = 0.4 \sim 0.6$ because of the larger apparent sizes of voids at lower redshifts.

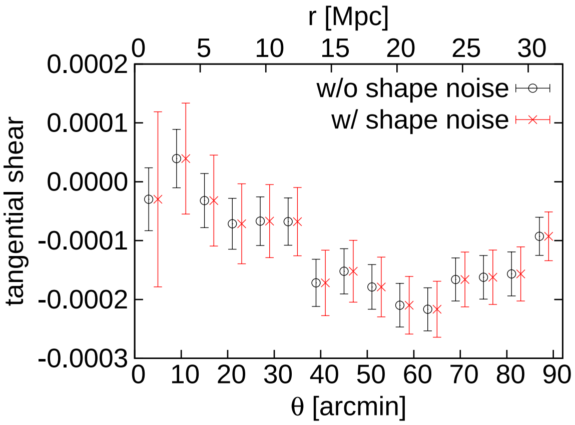

Figure 6. Crosses and circles with errors show the tangential shear profiles for the cases which include the shape noise and not. The staking analysis are carrie out for voids in the radial range $20 \leqslant R \leqslant 25$ Mpc. We assume a HSC-type survey, $n_g = 30$ arcmin^2, $\sigma_\epsilon = 0.4$ and FOV=5000 degree^2.

6.6 Comparison of the mass function of voids

In order to predict the mass function of voids analytically, we determine the linear density fluctuation δ_v from comparison of mass functions between the simulation and the modified PS theory (sec.4). In sec.6.3 and 6.4, masses of voids are estimated for each radius. From this and sec.6.1 the number count of voids is obtained as a function of mass. We set δ_v as a free parameter. Fitting is performed in the parameter range $0.1 \leqslant |\delta_v| \leqslant 1.0$.

In order to obtain the mass function in each radius from the simulation, we use masses estimated from the tangential shear profiles (sec.6.4). Because the inaccuracies of mass estimation from weak lensing signals affect the mass function, we fit masses with the function as

$$M = A_0 R^3, \tag{35}$$

where A_0 is constant and set as a free parameter. Fig.7 shows the relation between masses and radius estimated from void finder and the best-fit curve. From the least-square method, A_0 is determined as

$$A_0 = 1.32 \times 10^{11}. \tag{36}$$

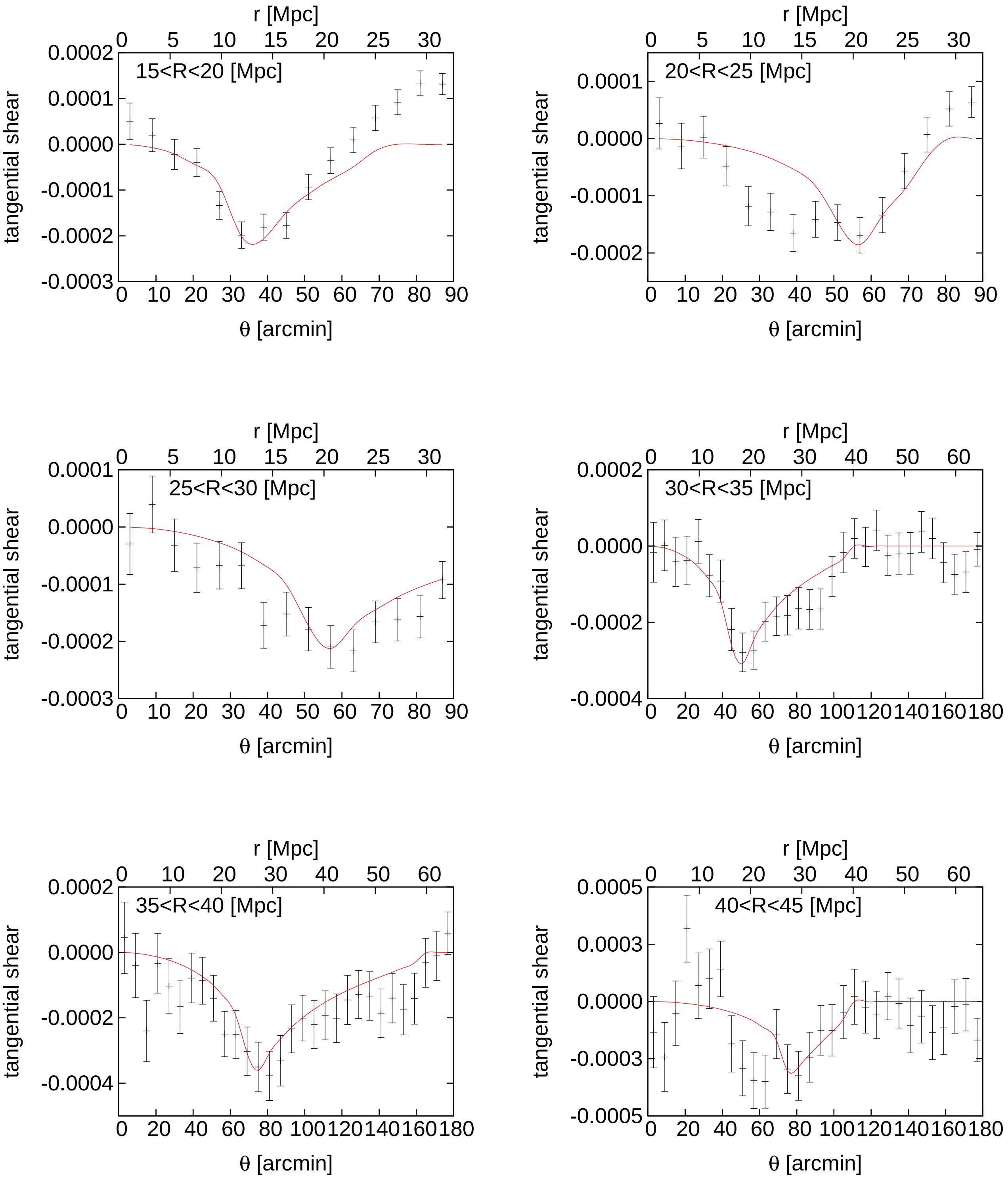

Figure 5. Tangential shear profiles estimated from simulation (points with errors), the best-fit double top-hat model (solid lines) in each radius. Same assumptions in fig.4 are adopted. Stacking analysis are carried out in each radius derived from the void finder; $15 \leqslant R \leqslant 20$ Mpc (*top-left*); $20 \leqslant R \leqslant 25$ Mpc (*top-right*); $25 \leqslant R \leqslant 30$ Mpc (*middle-left*); $30 \leqslant R \leqslant 35$ Mpc (*middle-right*); $35 \leqslant R \leqslant 40$ Mpc (*bottom-left*); $40 \leqslant R \leqslant 45$ Mpc (*bottom-rihgt*). Best-fit parameters are summarized in table.3.

Table 3. Best-fit parameters and derived total void mass. These parameters are determined from tangential shear profiles. Column (1): radius of void determined with the void finder; Column (2): density contrast; Column (3): radius of underdense region; Column (4): radius of overdense region; Column (5): void mass derived from the double top-hat model

Radius in the void finder [Mpc]	δ	$D_l\theta_1$ [Mpc]	$D_l\theta_2$ [Mpc]	Void mass [$M_\odot$]
$15 \sim 20$	-0.398	12.2	25.3	1.53×10^{15}
$20 \sim 25$	-0.170	19.1	27.6	2.50×10^{15}
$25 \sim 30$	-0.250	19.0	109	3.63×10^{15}
$30 \sim 35$	-0.403	16.8	40.0	4.00×10^{15}
$35 \sim 40$	-0.290	25.5	59.8	1.01×10^{16}
$40 \sim 45$	-0.183	27.3	39.5	7.80×10^{15}

Table 4. Signal-to-noise ratio, integrated over angular scales considered in the redshift range $z = 0.4 \sim 0.6$. (1): radius of void determined with the void finder; Column (2): the number count of voids in the each radial bin and the redshift range $z = 0.4 \sim 0.6$; Column (3): S/N derived from convergence; Column (4): S/N derived from tangential shear without the shape noise; Column (5): S/N derived from tangential shear with the shape noise; Column (6): S/N for one void. It is estimated from information of tangential shear with shape noise and the number of voids (table.1)

Radius [Mpc]	Number of voids	S/N (convergence)	S/N (tangential shear w/o shape noise)	S/N (tangential shear w/ shape noise)	$(S/N)/\sqrt{N_{void}}$ (w/ shape noise)
$15 \sim 20$	5246	11.7	11.0	9.18	0.127
$20 \sim 25$	3892	9.60	8.25	6.97	0.112
$25 \sim 30$	2446	8.65	7.55	6.51	0.132
$30 \sim 35$	1400	8.17	8.19	6.76	0.181
$35 \sim 40$	724	8.08	7.57	6.25	0.232
$40 \sim 45$	320	7.63	7.89	5.39	0.301

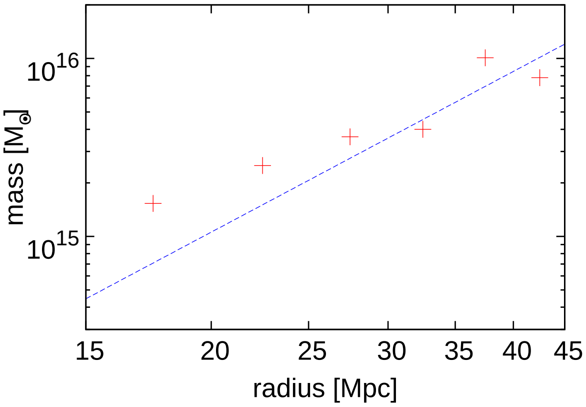

Figure 7. Mass-radius relation. x-axis is radius obtained from void finder. y-axis is mass estimated from our model with tangential shear profiles. Crosses show masses obtained from weak lensing signals and the dashed line plots best-fit curve with eq.35.

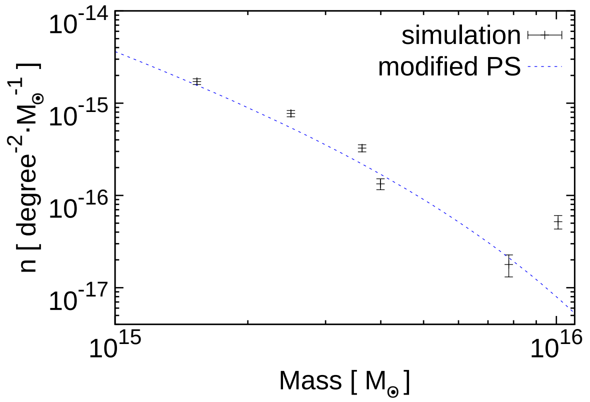

Figure 8. Mass function of voids in simulation and the modified PS theory. Points with errors show mass function of voids derived from the simulation. Masses are estimated from tangential shear profiles. The number count of voids in the redshift range $0.4 \leqslant z \leqslant 0.6$ are used. Error bar shows 1σ of the number count with 200 realizations. The dashed line shows the best-fit curve in the modified PS theory. The linear density fluctuation $\delta_v = -0.35$ is adopted.

Using eq.35, we divide the number count obtained from simulation by masses included in each radius range. The number count of voids is used in the redshift range $0.4 \leqslant z \leqslant 0.6$.

Figure.8 shows the mass function in the simulation and the best-fit curve of the mass function in the modified PS theory. Mass functions of voids in simulation are reproduced with $\delta_v = -0.35$. For checking the consistency, we also do same works for the case of convergence. The best-fit linear density becomes as $\delta_v = -0.5$ in that case. These values are smaller than the value predicted from the spherical top-hat model (Sheth & van de Weygaert 2004). From our result, however, the linear density parameter is sensitive to the mass estimation reconstructed from weak lensing signals. For better understanding, we should study structures of voids and ridges more carefully.

Table 5. Signal-to-noise ratio, integrated over angular scales considered in the redshift range $z = 0.1 \sim 0.3$. Column (1): radius of void determined with the void finder; Column (2): the number count of voids in the each radial bin and the redshift range $z = 0.1 \sim 0.3$; Column (3): S/N derived from convergence; Column (4): S/N derived from tangential shear without the shape noise; Column (5): S/N derived from tangential shear with the shape noise; Column (6): S/N for one void

Radius [Mpc]	Number of voids	S/N (convergence)	S/N (tangential shear w/o shape noise)	S/N (tangential shear w/ shape noise)	$(S/N)/\sqrt{N_{void}}$ (w/ shape noise)
$15 \sim 20$	1798	6.49	6.89	6.09	0.144
$20 \sim 25$	1097	5.73	5.69	5.22	0.158
$25 \sim 30$	523	7.36	7.21	6.70	0.293
$30 \sim 35$	252	5.65	5.09	4.43	0.279
$35 \sim 40$	88	6.93	6.62	5.67	0.605

7 CONCLUSION

In this paper, we have presented the observability of voids with stacked weak lensing in next generation surveys such as HSC. We select voids with a void finder from halo catalogue made from a large set of N-body simulations. We have stacked convergence and tangential shear profile for them with the full ray-tracing simulations to obtain an average dark matter profile (black in fig.4 and fig.5). From our stacking analysis, we have seen both structures of void and ridge outside the void. At small radii, the void finder cannot find true voids if the minimum radius ξ is set to small value. This result is consistent with the previous paper (Foster & Nelson 2009). In oder to predict the mass function of voids analytically, we compare the mass function of voids in the simulation with the modified PS theory and found that the modified PS theory can predict the mass function of voids obtained from the analysis for tangential shear profiles when the threshold linear density fluctuation is set to $\delta_{\rm v} = -0.35$. In addition, we have estimated total S/N, which indicates that stacked lensing signals from voids can be detected at significant level (S/N$\geqslant$ 5) for the 5000 degree^2 area, even if the error coming from the shape noise is added. The shape noise error becomes a dominant component at only small scale.

To fit lensing signals in stacked analysis, we have considered a simple void model called double top-hat model. Our model fits both profiles of convergence and tangential shear in simulation very well (fig.4 and fig.5). Estimated total void masses from this model were $M = 10^{14} \sim 10^{16} M_\odot$, which were a few times larger than masses derived from direct integration of the convergence profile at $\kappa(\theta) < 0$. We have confirmed that the dense ridges outside voids affect profiles of weak lensing signals and the mass estimation of voids. Therefore we have to take account of this effect for interpreting stacked weak lensing signals around voids. The underdense region is smaller than radius derived from the void finder, presumably because the halo catalogue used for finding voids does not trace true dark matter distributions directly.

Our work has demonstrated the observability of voids with the stacked weak lensing method. We have also suggested a simple model to interpret the lensing signals. In this work, the average number density of halos is 200 /degree$^2/\Delta z = 0.1$ in the redshift range $z = 0.4 \sim 0.5$. In the SDSS-III Baryon Oscillation Spectroscopic Survey (BOSS) (Dawson et al. 2012), the average number density of luminous red galaxies (LRG) is about 50 /degree$^2/\Delta z = 0.1$ in the same redshift range. From eq.19, void radii we can find mainly depend on the average distance between galaxies. In the simulation, it becomes about 6.86 Mpc. In BOSS, it becomes about 10.9 Mpc, which is about a factor of two larger than the average distance used in this work. However, it would be possible to find voids from the BOSS data which have large radii, and adopt techniques described in this paper using weak lensing measurements in e.g. HSC data. These techniques can also be applied to next generation surveys such as Euclid (Laureijs et al. 2011), Dark Energy Survey (DES) (The Dark Energy Survey Collaboration 2005) and Large Synoptic Survey Telescope (LSST) (LSST Science Collaboration et al. 2009).

When we were writing this paper, we came across a paper by Krause et al. (2012) which also studied stacked weak lensing signals around voids. The main difference of their paper from our analysis is that Krause et al. (2012) assumed analytic mass profiles to estimate S/N, while in this paper we present realistic stacked lensing profiles and the error covariance with ray-tracing of N-body simulations. In addition, Krause et al. (2012) considered voids with smaller radii of $\leqslant 15h^{-1}$Mpc for which our void finder does not work well. Nevertheless, by extrapolating both the results we argue that they are broadly consistent with each other.

ACKNOWLEDGMENTS

We would like to thank Masanori Sato for proveding the raytracing data and Yosuke Utsumi, Tsz Yan Lam, Masahiro Takada for useful discussions and comments. We also thank Caroline Foster for making the code VoidFinder freely available. Numerical computations in the paper were in part carried out on the general-purpose PC farm at Center for Computational Astrophysics, CfCA, of National Astronomical Observatory of Japan. This work was supported in part by the FIRST programme eSubaru Measurements of Images and Redshifts (SuMIRe)f, World Premier International Research Center Initiative (WPI Initiative), MEXT, Japan, and Grant-in-Aid for Scientific Re- search from the JSPS (23740161), and in part by Grant-in-Aid for Scientific Research from the JSPS Promotion of Science (23540324, 23740161)

REFERENCES

Amendola L., Frieman J. A., Waga I., 1999, MNRAS, 309, 465

Bardeen J. M. et al., 1986, ApJ, 304, 15
Bartelmann M., Schneider P., 2001, Physical Rep., 340, 291
Broadhurst T. et al., 2005, ApJ, 619, L143
Clowe D. et al., 2000, ApJ, 539, 540
Colberg J. M. et al., 2008, MNRAS, 387, 933
Dawson K. S. et al., 2012, ArXiv e-prints: 1208.0022
Fahlman G. et al., 1994, ApJ, 437, 56
Fillmore J. A., Goldreich P., 1984, ApJ, 281, 9
Foster C., Nelson L. A., 2009, ApJ, 699, 1252
Furlanetto S. R., Piran T., 2006, MNRAS, 366, 467
Hamana T., Mellier Y., 2001, MNRAS, 327, 169
Hoyle F. et al., 2005, ApJ, 620, 618
Hoyle F., Vogeley M. S., 2004, ApJ, 607, 751
Jain B., Van Waerbeke L., 2000, ApJ, 530, L1
Jones D. H. et al., 2004, MNRAS, 355, 747
Kamionkowski M., Verde L., Jimenez R., 2009, JCAP, 1, 10
Kirshner R. P. et al., 1981, ApJ, 248, L57
Klypin A. et al., 1999, ApJ, 522, 82
Krause E. et al., 2012, ArXiv e-prints: 1210.2446
Laureijs R. et al., 2011, Arxiv
Lee J., Park D., 2009, ApJ, 696, L10
Li B., Zhao G.-B., Koyama K., 2012, MNRAS, 421, 3481
LSST Science Collaboration et al., 2009, ArXiv e-prints: 0912.0201
Mandelbaum R. et al., 2006, MNRAS, 372, 758
Miyazaki S. et al., 2002, ApJ, 580, L97
Miyazaki S. et al., 2006, in SPIE, Vol. 6269, Society of Photo-Optical Instrumentation Engineers (SPIE) Conference Series
Moffat J. W., 2006, JCAP, 5, 1
Oguri M. et al., 2012, MNRAS, 420, 3213
Oguri M., Takada M., 2011, Phys. Rev. D, 83, 023008
Okabe N. et al., 2010, PASJ, 62, 811
Pan D. C. et al., 2012, MNRAS, 421, 926
Park D., Lee J., 2007, Phys. Rev. Let., 98, 081301
Peebles P., 1980, The large-scale structure of the universe
Prada F. et al., 2012, MNRAS, 423, 3018
Press W. H., Schechter P., 1974, ApJ, 187, 425
Rozo E. et al., 2010, ApJ, 708, 645
Ryden B. S., Turner E. L., 1984, ApJ, 287, L59
Sato M. et al., 2009, ApJ, 701, 945
Sheth R. K., van de Weygaert R., 2004, MNRAS, 350, 517
Spergel D. N. et al., 2007, ApJS, 170, 377
Springel V., 2005, MNRAS, 364, 1105
Squires G. et al., 1996, ApJ, 469, 73
Squires G. et al., 1997, ApJ, 482, 648
Strauss M. A. et al., 1992, ApJ, 385, 421
Suto Y., Sato K., Sato H., 1984, Progress of Theoretical Physics, 71, 938
Takada M., 2006, Phys. Rev. D, 74, 043505
Tavasoli S., Vasei K., Mohayaee R., 2012, ArXiv e-prints: 1210.2432
The Dark Energy Survey Collaboration, 2005, ArXiv Astrophysics e-prints: 0510346
Umetsu K. et al., 2011, ApJ, 738, 41
Van Waerbeke L. et al., 2000, A&A, 358, 30
White M., Hu W., 2000, ApJ, 537, 1